Supplementary Information for

Adaptive continuous-shape-changing solar-powered microfliers

Haoyang Sun[1], Chenxi Yang[1], Zhenlong Wang[1], Yifan Wang[1], Xinrui Zhang [1],

Yunhao Ren[1], Wenhua Li[1], Honglong Chang[1], Kan Li[2], YongAn Huang[2], Binghe Ma[1],

Weizheng Yuan[1], Tao Ye[1]*

[1]Ministry of Education Key Laboratory of Micro/Nano Systems for Aerospace, Key Laboratory of Micro- and Nano-Electro-Mechanical Systems of Shaanxi Province, School of Mechanical Engineering, Northwestern Polytechnical University, Xi'an 710072, China

[2]State Key Laboratory of Digital Manufacturing Equipment and Technology, Flexible Electronics Research Center, Huazhong University of Science and Technology, Wuhan 430074, China

*Corresponding author: yetao@nwpu.edu.cn

The PDF file includes:

Supplementary Notes 1 to 5

Supplementary Figs. 1 to 11

Other Supplementary Material for this manuscript includes the following:

Supplementary Movies 1 to 5

Supplementary Note

1. The continuous-shape-changing mechanism analyses

According to the excellent characteristics of SMAs (lightweight, trigger sensitivity, and rapid continuous actuation force), the SMAs were used as S-shape and 2S-shape actuators for heterogeneous integration within microfliers to perform adaptive continuous-shape-changing. The continuous-shape-changing and recovery of SMAs are driven by the unique reversible phase transition between martensite and austenite phases, where external forces or temperature variations induce shape deformations, which are then restored to its original form through phase transformation. This one-way SMA returns to its preset shape upon heating, but does not automatically revert to its deformed state upon cooling, thereby significantly simplifying the programming complexity. According to Joule's law, when an electric current flows through an SMA, heat is generated, as described by the following equation:

$$Q = I^2 R t$$

Where Q is the generated heat, I is the current flows through the SMA, R is the electrical resistance of the SMA, and t is the duration of current. The temperature change (ΔT) of the SMA can be determined from the generated heat and the material thermal properties, as expressed by the following equation:

$$\Delta T = \frac{Q}{mc}$$

Where m is the mass of the SMA and c is the specific heat capacity of the material. Substituting the expression for Q into the temperature change equation yields:

$$\Delta T = \frac{I^2 R t}{mc}$$

This formula expresses the relationship between ΔT and I, R, t, m, and c. The temperature change directly influences the phase transition of the SMA and drives the

42 shape change. As the temperature increases, the SMA changes from the martensite phase

43 to the austenite phase and induces shape-changing of microflier. Conversely, as the

44 temperature decreases, the SMA changes back from the austenite phase to the martensite

45 phase and recoveries to the original shape.

46 The shape-changing angle of SMA can be fine-tuned through precise adjustment of

47 the current intensity and duration, therefore, it is possible to control the shape-changing

48 behavior of the SMAA-based microflier by adjusting these parameters, achieving desired

49 angles for functional applications in various environments. Based on the above analyses,

50 we can conclude that under ideal conditions (without heat dissipation), once the SMAA

51 parameters are selected, we can control the degree of shape-changing (θ) by adjusting t

52 and I. If we further consider actual heat dissipation conditions and establish a transient

53 thermal equilibrium equation, which will lead to more precise control of the SMAA.

54 However, in practical applications, the wind field was more complex, and the heat

55 dissipation conditions were variable. Thus, we performed idealized analyses and employed

56 empirical measurement methods to provide the relationship between the duration of current

57 applied and the shape-changing angle with a fixed current intensity (Fig. 2f).

58 **2. SMAA-EAM actuating system**

59 The SMAA-EAM actuating system integrated a network of multi-modal sensors to real-

60 time detect external environmental parameters such as temperature and pressure variations.

61 It employed sensors to convert changes of external multi- environmental parameters into

62 electrical signals. Through pre-programmed algorithms and adaptive threshold logic, the

63 system analyzed signal patterns against predefined triggering criteria stored in the non-

64 volatile memory and enabled dynamic decision-making for actuating. Upon meeting

65 specific environmental thresholds, the phase transformations of SMAAs could be precisely

66 controlled through Joule's law, generating precise longitudinal shape-changing of

67 microflier in response to different environmental conditions. The EAM did not consume

68 energy from the microflier power and it was powered by the drone power supply, which

also provided electricity to the SMAA for adaptive continuous-shape-changing. The electric energy was transmitted between the EAM and SMAA through 36 AWG wires, and the microflier was not affected when dispersal into the air and then released by gravity. We used modular integration technology to generate rapid iterative prototypes to achieve the necessary functions. EAM could also be further miniaturized to improve portability and integration.

A key advantage of the proposed microfliers was the integration of SMAA. With customizable dimensions and memory effects, SMAA provided flexibility and controllability to surpass the binary-state magnetic actuators in current origami microfliers. Notably, controlled power modulation enabled continuous-shape-changing of SMA via phase transformation kinetics. Furthermore, SMAA provided an additional significant advantage: its bio-inspired curved attachment ensured the microflier maintained an optimal angle for both wind dispersions and post-landing states (orientations). This design ensured that the solar cells in the microflier could maximize the sunlight capture and prevented disruptions in energy collection due to suboptimal landing orientations. As a result, issues related to insufficient power supply caused by variations in sunlight exposure of on-site solar cells within the microfliers are effectively mitigated.

3. Electronic component selection for flexible solar-powered wireless circuits

The flexible solar-powered wireless circuits consisted of two parts: the solar power management circuit module and the multi-parameter sensing and communication circuit module. Specifically, the solar power management circuit module was composed of a micro diode, two LDOs (2.5 V, 1.9 V), CAP (2.5 V, 11 mF), resistors (1 kΩ), and capacitors (100 μF). We considered the maximum voltage that the core electronic components of the circuit could handle, and then solar energy management was implemented using diodes and LDOs. The supercapacitor was used to store charge, which could mitigate fluctuations in solar energy and ensure the stable operation of the entire circuits. Resistors were used to

divide the voltage and control the voltage of the supercapacitor, ensuring that the supercapacitor reached sufficient voltage before triggering the LDO to supply power to the subsequent multi-parameter sensing module. In summary, sufficient electrical energy was provided by the solar power management circuit module and ensured the normal operation of microflier electronical components under ambient conditions.

The multi-parameter sensing and communication circuit module was centered around a Bluetooth microcontroller (NRF52832) and high-precision temperature and pressure sensors (BMP384). The circuit module used a low-power Bluetooth chip and integrated peripheral components, including filter capacitors, inductors, and an external crystal oscillator. It connected to sensors via communication interfaces such as GPIO, I^{2}C, and SPI, enabling logic control and data collection. The design also included a surface-mount ceramic antenna with impedance matching components to meet the requirements for compact size and low weight. The integrated BMP384 sensor featured compact packaging to reduce system weight and offered electrostatic discharge resistance and high robustness, ensuring stable monitoring of environmental factors. Both sensors supported multiple communication interfaces for simple integration with the Bluetooth microcontroller. In summary, the multi-parameter sensing circuit module connected to the Bluetooth microcontroller, powered by the solar power management circuit module, could enable real-time sensing and long-distance data transmission of various environmental parameters (e.g., temperature and pressure).
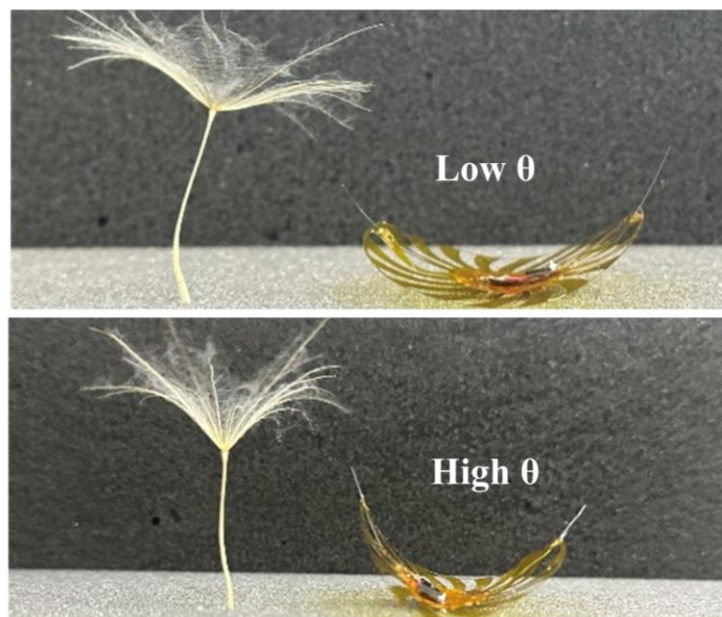
4. Electrical performance experiments

The solar simulator provided more stable and accurate light source for the measurements of microflier electrical performance as compared to fluctuating outdoor light. We tested the start-up phase of microflier after the light was turned on. Specifically, the microflier was placed at the center of the light simulator beam and the light intensity received by the microflier during this process was calibrated using a light power meter. Two digital source

123 meters (2450 Sourcemeter, Keithley) were used to simultaneously measure the voltages of

124 solar cell, CAP, MCU through three channels. Voltage variations of the microflier (with the

125 solar cell facing upward) were plotted from dark to a light intensity of ~803 W·m^{-2} (Fig.

126 4c). Additionally, we tested start-up time of the MCU under different 5 light intensities

127 (~200 W·m^{-2}, 300 W·m^{-2}, 400 W·m^{-2}, 600 W·m^{-2}, and 800 W·m^{-2}). Specifically, we

128 performed the same measurement described above using a source meter connected between

129 the solar cells and the circuit input during the start-up phase and defined that the start-up

130 time was the moment MCU received signals. Light intensities were recorded by a light

131 power meter and time required to start the MCU were recorded by a source meter. For each

132 group of light intensity, three independent experiments were conducted and the data were

133 averaged. The corresponding results are plotted in Fig. 4d.

134
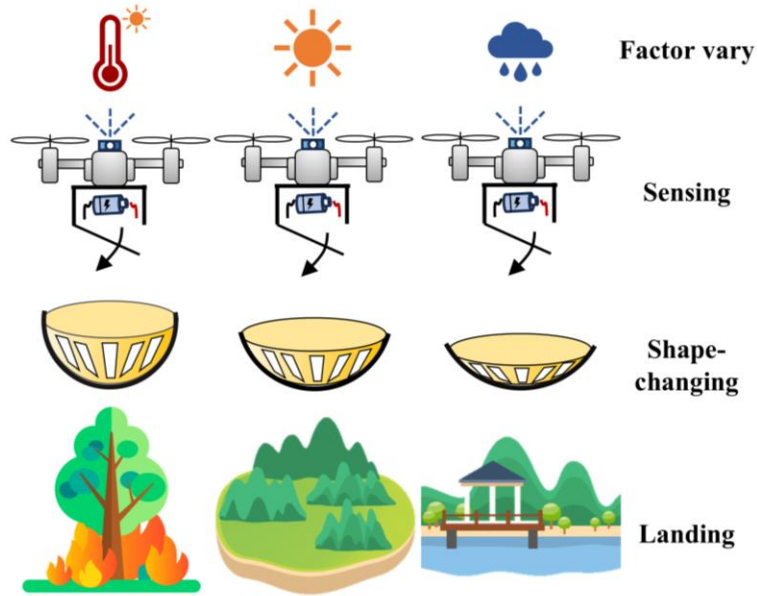
135 **5. Outdoor environmental monitoring tests**

136 To evaluate the adaptive continuous-shape-changing capability of the microflier in ambient

137 conditions, temperature was chosen as the environmental factor, and dispersion monitoring

138 experiments were conducted in areas with different temperature conditions. The adaptive

139 response of microflier was programmed as follow: when the environmental temperature T

140 ≤ 10 °C, it maintained a predefined large angle, while at $T \geq 10$ °C, the SMAA activated to

141 drive the microflier to flatten its angle. Two areas were selected for the experiment: a sunny

142 area (warm area), where the temperature remained above 10 °C, and a cooler area (cold

143 area), where the temperature stayed below 10 °C. Upon deployment of the microflier by

144 the drone in the warm area, the microflier successfully deformed to a flat angle due to the

145 braking mechanism. In contrast, when deployed in the cold area, no deformation occurred,

146 and the microflier maintained its original large angle. After landing, the Bluetooth

147 microcontroller activated and the microflier sensed signal was connected to a ground

148 station via wireless communication, the monitoring data packets (2 min per packet) were

149 received from approximately 20 meters away.

150   Additionally, to minimize the additional weight, we tested a version of the microflier

151   that integrated flexible solar-powered wireless circuit and successfully conducted outdoor

152   experiments (Fig. 5d). The results indicated that the designed microflier could monitor

153   multiple environmental parameters. Four typical deployment scenarios (forest, brushwood,

154   hill, and road) were chosen (Supplementary Fig. 10) for the continuous monitoring

155   measurements of three important environmental parameters (temperature and pressure).

156   Finally, a lawn was selected for long-term monitoring to fully demonstrate the monitoring

157   potential of the microfliers. A week-long environmental monitoring experiment was

158   conducted with the ground station to wirelessly transmit data in the same manner as before.

159   On the third and fourth days of the experiment, cloudy weather occurred with a recorded

160   light intensity of only 16.4 W m^{-2}. This caused a brief interruption in Bluetooth

161   communication; however, once sunlight resumed, the ground station successfully

162   reconnected to Bluetooth and resumed monitoring data receiving, the data were compiled

163   into weekly charts (Figs. 5e and 5f). The results demonstrated the microflier's ability to

164   adapt to different environmental conditions, monitor multiple parameters, and maintain

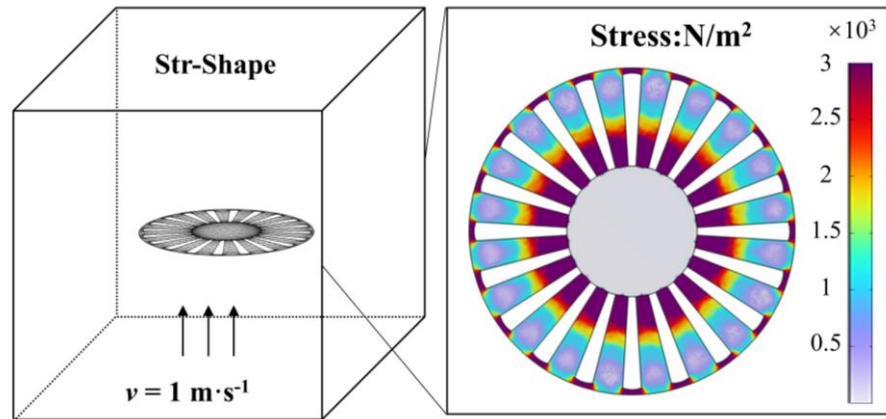165   reliable performance over long period even under dynamic conditions.

166

167

Supplementary Fig. 1. Saddle microflier. Images show that the microflier, like the dandelion seed, can achieve shape-changing with low and high angles (θ).
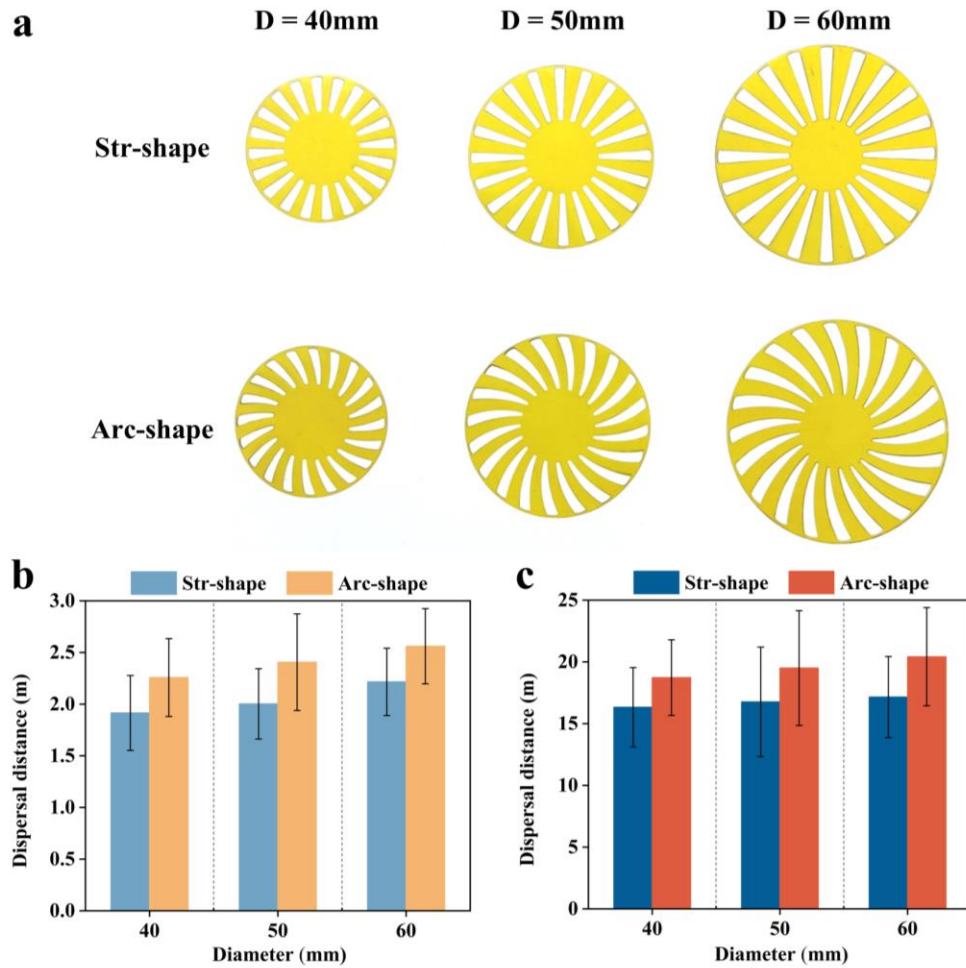
170

Supplementary Fig. 2. Intelligent deployment processes of microfliers. The EAMs on minidrones sense different environmental factors and drive SMAAs to enable continuous-shape-changing of microfliers to adjust the flight performances and landing points for monitoring specific environmental conditions.
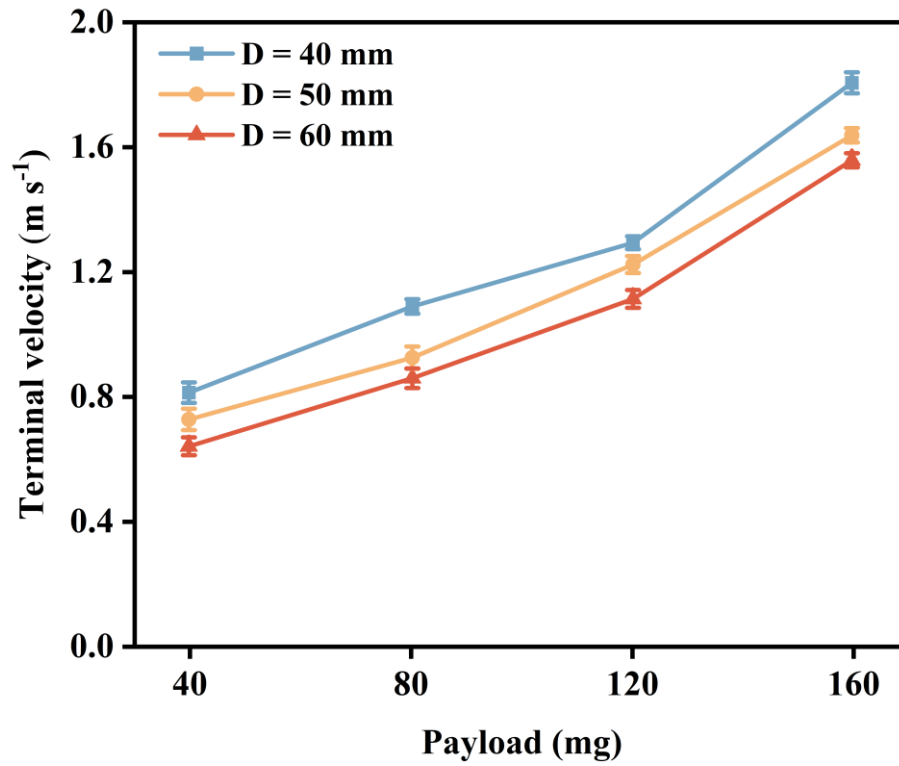
175

Supplementary Fig. 3. Modeling and simulation of str-shape aerodynamic structure. The simulated stress field distribution of the straight aerodynamic structure under under longitudinal wind filed. Compared to the arc-shape aerodynamic structure, the stress field distribution of str-shape aerodynamic structure is more uniform, so the spinning tendency should be reduced during flight.
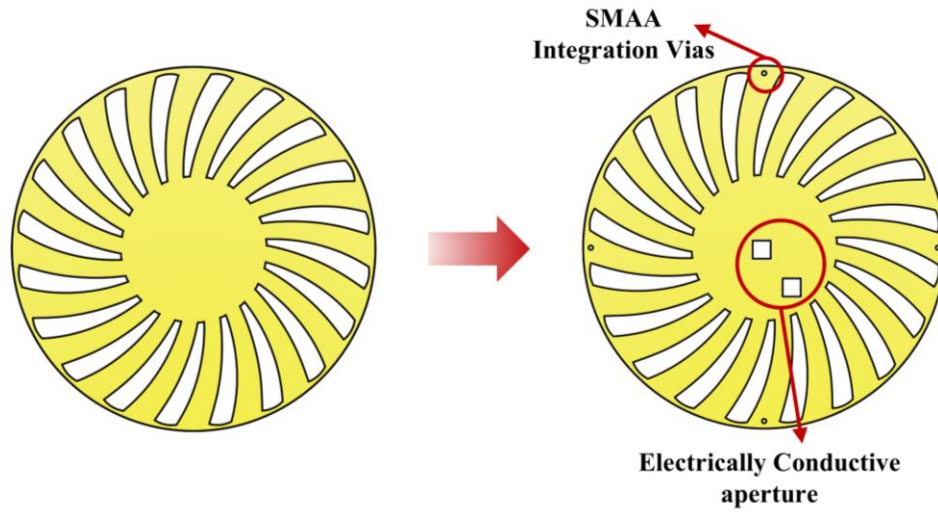
181

Supplementary Fig. 4. Designs and dispersal distances of aerodynamic structures with different sizes and patterns. a Aerodynamic structures with different sizes and patterns. **b** Dispersal distances of aerodynamic structures with different sizes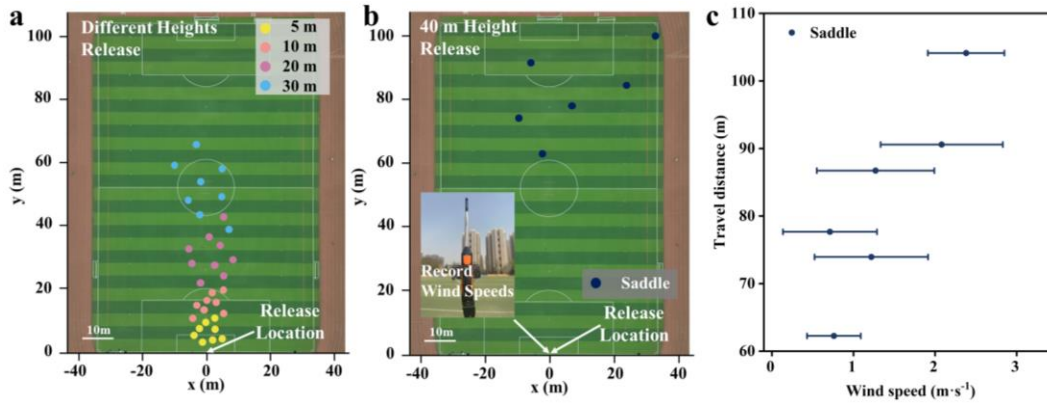 and patterns when outdoor deployed at a height of 2 meters. **c** Dispersal distances of aerodynamic structures with different sizes and patterns when outdoor deployed at a height of 10 meters.

187

Supplementary Fig. 5. Payload capacity. The terminal velocities of aerodynamic structures with three different diameters (40 mm, 50 mm, and 60 mm) under different weights of approximately 40 mg, 80 mg, 120 mg, and 160 mg.
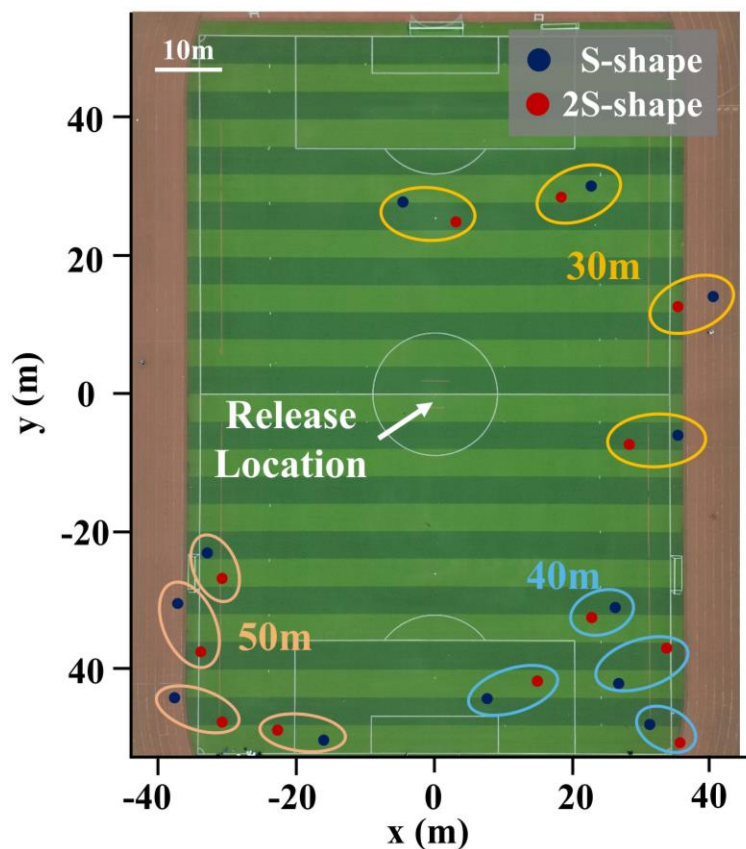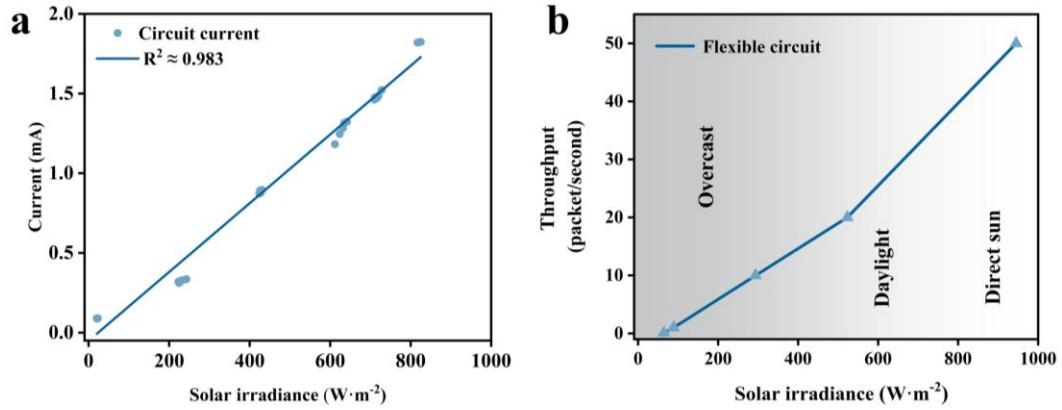
191

Supplementary Fig. 6. Aerodynamic layer structure optimization. The optimized bionic aerodynamic layer featured SMAA integration bias and electrically conductive aperture to improve the integrability of microflier, these designs could eliminate redundant jump wires.
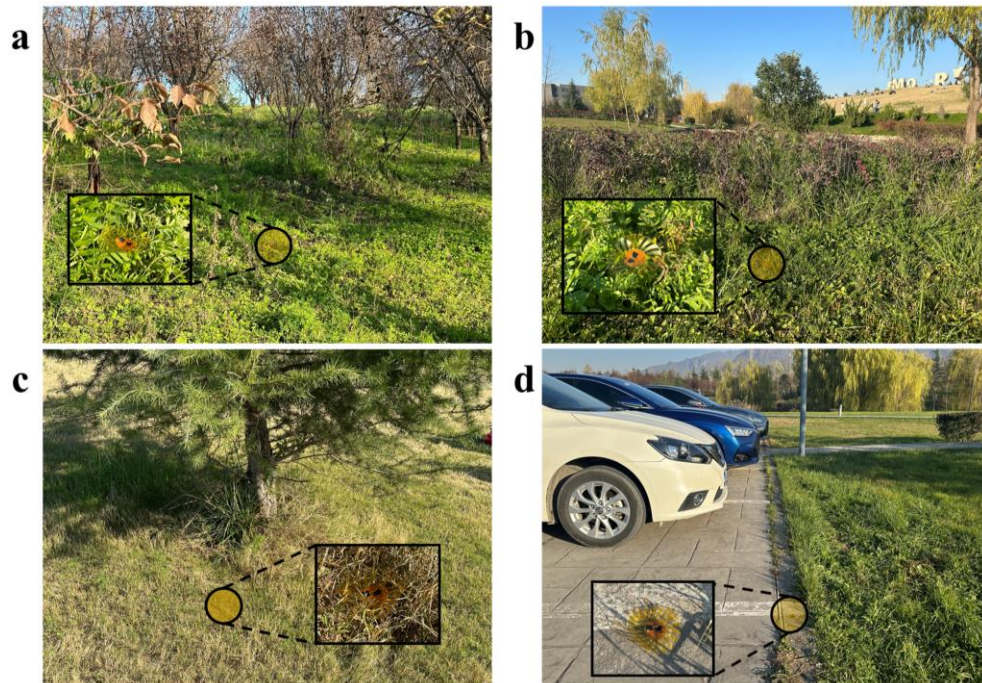
Supplementary Fig. 7. Wind dispersal distance tests. a The saddle microfliers are released at different heights (5 m, 10 m, 20 m, 30 m), and their landing points are recorded on an aerial map ($N \geq 8$ drop trials). **b** The saddle microfliers are released at 40 m height, and their landing points are recorded on an aerial map with wind speeds were recorded by a hot wire anemometer ($N = 6$ drop trials). **c** Wind speeds versus travel distances for 40 m height drop measurements (error bars indicate $\pm\sigma$, $N \geq 30$ wind measurements).
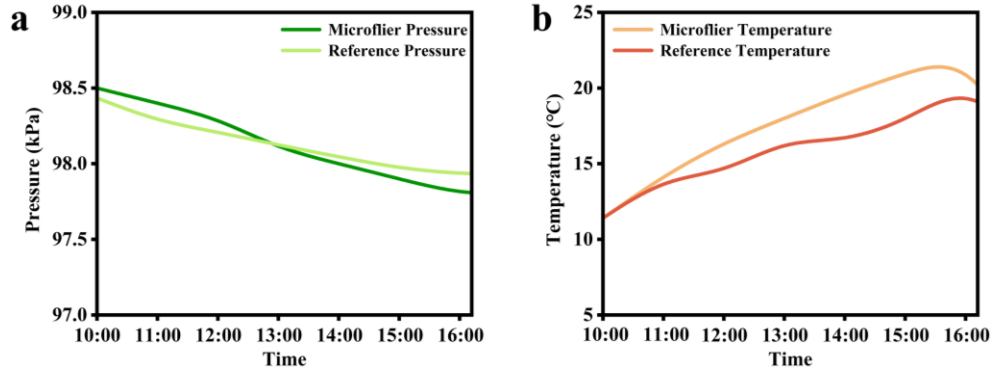
203

Supplementary Fig. 8. Comparison of the actual landing points of the saddle and hemisphere microfliers, as shown in Fig. 3g. Landing positions of saddle and hemisphere microfliers after being released at heights of 30 meters, 40 meters, and 50 meters ($N = 4$).

Supplementary Fig. 9. Solar irradiances to currents and throughputs. a Currents harvested from two solar cells at different light intensities. We apply linear regression to obtain a mapping with $R^2 \geqslant 0.983$ ($N \geq 20$). **b** Achievable Bluetooth throughput under different light intensities ($N = 3$, $\pm\sigma$).

212

213 **Supplementary Fig. 10. 4 environments for environmental factors monitoring.** These

214 images showed that microfliers self-sustaining monitored the environment factors in forest,

215 brushwood, hill, and road conditions.

216

Supplementary Fig. 11. Sensor evaluation. a The pressure recorded by the microflier sensor at hourly intervals from 10:00 am to 16:00 pm, compared with the pressure curve recorded by the meteorological station at the same times, the error is $\delta \leq 5\%$. **b** After applying coefficient correction to account for self-heating interference, the temperature recorded by the microflier sensor at hourly intervals from 10:00 am to 16:00 pm, compared with the temperature curve recorded by the meteorological station at the same times, the error is $\delta \leq 15.94\%$.